JACS
JOURNAL OF THE AMERICAN CHEMICAL SOCIETY
ARTICLE
pubs.acs.org/JACS

# Imaging Secondary Structure of Individual Amyloid Fibrils of a $\beta_2$-Microglobulin Fragment Using Near-Field Infrared Spectroscopy

Melissa Paulite,[†] Zahra Fakhraai,[†] Isaac T. S. Li,[†] Nikhil Gunari,[‡] Adrienne E. Tanur,[†] and Gilbert C. Walker*[,†,‡]

[†]Department of Chemistry, University of Toronto, Toronto, Ontario, Canada M5S 3H6

[‡]Department of Chemistry, University of Pittsburgh, Pittsburgh, Pennsylvania 15260, United States

S Supporting Information

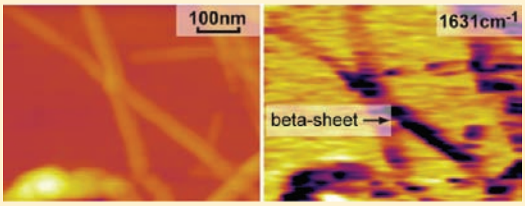

**ABSTRACT:** Amyloid fibril diseases are characterized by the abnormal production of aggregated proteins and are associated with many types of neuro- and physically degenerative diseases. X-ray diffraction techniques, solid-state magic-angle spinning NMR spectroscopy, circular dichroism (CD) spectroscopy, and transmission electron microscopy studies have been utilized to detect and examine the chemical, electronic, material, and structural properties of amyloid fibrils at up to angstrom spatial resolution. However, X-ray diffraction studies require crystals of the fibril to be analyzed, while other techniques can only probe the bulk solution or solid samples. In the work reported here, apertureless near-field scanning infrared microscopy (ANSIM) was used to probe the secondary structure of individual amyloid fibrils made from an in vitro solution. Simultaneous topographic and infrared images of individual amyloid fibrils synthesized from the #21−31 peptide fragment of $\beta_2$-microglobulin were acquired. Using this technique, IR spectra of the amyloid fibrils were obtained with a spatial resolution of less than 30 nm. It is observed that the experimental scattered field spectrum correlates strongly with that calculated using the far-field absorption spectrum. The near-field images of the amyloid fibrils exhibit much lower scattering of the IR radiation at approximately 1630 cm$^{-1}$. In addition, the near-field images also indicate that composition and/or structural variations among individual amyloid fibrils were present.

## INTRODUCTION

Amyloid fibril formation results from the anomalous folding and aggregation of proteins and is associated with many neurodegenerative diseases such as Alzheimer's[1] and Creutzfeldt−Jakob[2,3] diseases, as well as physically debilitating ailments such as carpal tunnel syndrome. In particular, $\beta_2$-microglobulin ($\beta_2$-m) amyloid fibril formation is detected in patients suffering from chronic renal failure while undergoing hemodialysis.[4] $\beta_2$-m amyloidosis occurs when the $\beta_2$-m protein accumulates in high concentrations, thus forming amyloid fibrils that collect pathogenically in body joints. All amyloid fibrils, including those of $\beta_2$-m, share three similar physical characteristics. First, these fibrils comprise a high percentage of $\beta$-sheet structure in a "cross-$\beta$" pattern where the $\beta$-strands are perpendicular to the long axis of the fibril and have been visualized using X-ray diffraction techniques.[5] Second, amyloid fibrils are typically smooth and exhibit unbranched structures micrometers in length. It has been observed under electron microscopy[6,7] that most amyloid fibrils synthesized from various proteins consist of several protofilaments that wrap in bundles to form the mature fibril. Last, these fibrils have the ability to allow a dye such as Congo red to intercalate between the $\beta$-sheets, wherein green-gold birefringence is observed under cross-polarized optical microscopy.[8]

Several studies have identified the particular primary sequences within the $\beta_2$-m protein that greatly contribute to its formation of amyloid fibrils.[4,9−11] In particular, the hydropathic #21−31 peptide ($^{21}$NFLNCYVSGFH$^{31}$) is a peptide fragment from the $\beta_2$-m core that is believed to play an important role in the protein's $\beta$-sheet conformation when in a fibril. Kozukh et al.[4] and Hiramatsu et al.[11] have shown that the pure #21−31 fragment when in a fibril adopts a mainly $\beta$-sheet configuration using IR linear dichroism spectroscopy. In addition, Hiramatsu et al. obtained detailed structural information on the local geometries of individual peptide groups of $\beta_2$-m. Infrared (IR) spectroscopy is a well-established tool used to investigate protein secondary structure by examination of the amide I and amide II bands.[12] Second derivative spectra of native $\beta_2$-microglobulin in $D_2O$ solution were also utilized to detect the structural properties of amyloid fibrils.[13] Hiramatsu et al.[14] used $^{13}$C isotope labeling of particular amino acids in the #21−31 fragment to deduce the secondary structure from amide I band frequency shifts. Such IR measurements on macroscopic quantities of material probe ensemble properties and any evidence of spatial heterogeneity on the length scale of individual fibrils is only indirectly obtained.

**Received:** October 15, 2010
**Published:** April 27, 2011

Apertureless near-field scanning IR microscopy (ANSIM) offers high spatial resolution imaging. It is a relatively new technique in which an impinging infrared beam is scattered by a sharp atomic force microscopy (AFM) tip oscillating at the resonant frequency of the cantilever in close proximity with a sample. The scattered light is then collected by an IR detector and is demodulated at this resonant frequency or its harmonics. In this way, the background scatter of the focused laser beam incident on the rest of the sample surface can be reduced and a spatial resolution far beyond the diffraction limit of light can be achieved to obtain infrared contrast with nanoscale spatial resolution.[15−17] Since the apex of the AFM tip is much smaller than the focal area of the laser beam, the scattered light is weak. To enhance this field, homodyne detection is used where a reference field is added to the backscattered signal field and the relative phase of the fields is set such that maximum constructive interference occurs at the IR detector. The scattering intensity is then proportional to the magnitude of the reference electric field.[18−20] An important consideration in near-field imaging is to avoid artifacts induced by the z-motion of the AFM tip.[21−25] It has previously been demonstrated by Mueller et al. that in the absence of large topographical features and with proper adjustment of the homodyne phase, this problem can be minimized. This technique is then reliably used to obtain the scattered field spectrum of materials with a spatial resolution of less than 30 nm.[15] The use of near-field scanning microscopy has been previously demonstrated for biological materials, particularly for macromolecules such as tobacco mosaic virus[26] and *E. coli* bacteria.[27]

In this paper, secondary structure information of amyloid fibrils formed from the #21−31 peptide fragment of $\beta_2$-m obtained by apertureless near-field scanning infrared microscopy (ANSIM) is reported. Near-field images were collected simultaneously with topography, enabling the detection and collection of the scattered field spectrum of individual fibrils on a gold substrate.

A number of different proteins undergo amyloid fibril formation through a process called nucleation-dependent polymerization.[28] This model invokes two phases: nucleation and linear extension by aggregation.[29,30] The first phase is a nucleus made from protein monomers that eventually grow into oligomers. This step is reversible and rate-limiting. At a critical mass, the addition of more peptide or protein to the nucleus or the addition of these nucleation sites to each other promotes growth. The kinetics of $\beta_2$-m amyloid fibril formation was studied[31−33] and described by the same polymerization model. It has been demonstrated that fibril formation can depend on a critical concentration of the protein for spontaneous fibril formation as well as on the reaction conditions including pH,[34] the addition of chaotropic agents, introduction of nanoparticles,[35] and mechanical agitation either by vortexing or shaking. In diseases such as carpal tunnel syndrome, it is the larger, ordered mature fibrils, rather than the small, disordered protofibrils, that are likely relevant to the pain symptoms. As a consequence, the conditions that lead to the growth of these mature fibrils are of interest.

Certain osmolytes are generally known to stabilize the native state of proteins. Osmolytes, such as TMAO, could act as a chemical chaperone, correcting folding defects by preferentially hydrating partially denatured proteins and entropically stabilizing native conformations.[36] It is believed that these osmolytes could stabilize the native state, which can be explained by their preferential exclusion from the protein surface, which is termed the osmophobic effect.[37] This effect is proportional to the solvent-exposed surface area of the protein; more expanded conformations are disfavored in the presence of osmolytes, and the protein tends to adopt the more compact native structure. In addition, Kim et al.[38] found that the interaction of certain osmolytes with proteins inhibits their conformational fluctuations within the native state of proteins and the increase of the free energy of unfolding makes it unfavorable for proteins to denature.

As a consequence, the role of osmolytes in inducing fibril formation is of interest. By monitoring the levels of TMAO using $^1$H NMR spectroscopy, Foxall et al.[39] established that patients suffering from renal transplant dysfunction produced levels of TMAO in their urine that were significantly higher than those found in healthy or successful post-transplantation patients. Furthermore, Schreiber[40] observed that TMAO is eradicated in patients with normal renal behavior. However, for patients undergoing renal failure and requiring hemodialysis, TMAO levels are higher than in those with normal renal function. Wishart[41] believed TMAO to be responsible for the body's management of the effects caused by increased amounts of protein denaturants such as urea and guanidine in patients who suffer from renal failure, as reflected in the elevated levels of this metabolite in those instances. Thus, there may be a physiological link between the presence of TMAO and $\beta_2$-amyloidosis, as accumulation of $\beta_2$-m and increased levels of TMAO are both observed in patients suffering from renal failure on dialysis.

There have been previous studies of TMAO's effect on fibril formation of other proteins and peptides[42−46] and promotion of microtubule assembly.[47] Yang et al.[36] studied the A$\beta$(1−40) peptide and found that as increasing concentrations of TMAO were added, the amount of $\beta$-sheet conformation appeared to reach a plateau, indicating that fibril formation can be independent of TMAO concentration. Gazit et al.[29] have reported results similar to those of Yang et al. wherein they observe an increase in the aggregation of peptides for different proteins upon the addition of TMAO. Thus, fibril formation was enhanced by the addition of TMAO, though the mechanism remains to be fully elucidated.

The fibrils reported on in this paper were formed in the presence of osmolyte trimethylamine *N*-oxide (TMAO). ANSIM was used to identify heterogeneity among *individual* fibrils.

## MATERIALS AND METHODS

**Sample Preparation.** The lyophilized, trifluoroacetic acid (TFA) #21−31 peptide was synthesized at the Center for Biotechnology and Bioengineering at the University of Pittsburgh and purified (>95%) by HPLC. Amyloid fibrils utilized for the near-field measurements were prepared by adding approximately 0.8 mg of TMAO (Sigma-Aldrich) to a solution of 1 mM #21−31 peptide using 18.2 M$\Omega$ water as the solvent (final pH 5.5), which is similar to a procedure performed by Yang et al.[36] Ultraflat gold substrates[48] were produced for the near-field measurements. Approximately 40 $\mu$L of the solution aged for 1 month at room temperature was deposited for 2−3 min onto fresh ultraflat gold substrates, briefly rinsed with a stream of 18.2 M$\Omega$ water and dried with flowing $N_2$ gas. The sample was then placed in the ANSIM instrument.

Two different 1 week old fibril solutions were used for Fourier transform infrared (FTIR) measurements. One solution was produced using 1.3 mg of peptide (1 mM) dissolved in 1 mL of 18.2 M$\Omega$ water, and its pH was adjusted with 120 mM NaOH to a final value of pH 5.5. The other fibril solution was made identically to the solution prepared as described previously for near-field measurements, final pH 5.5.

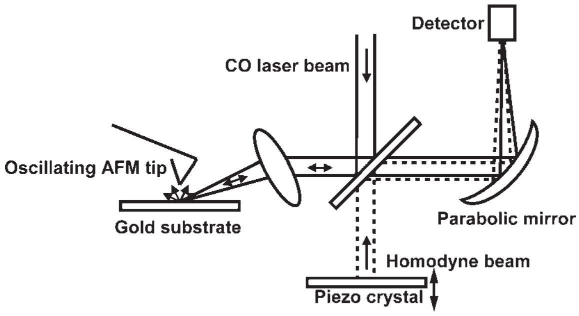

**Figure 1.** Schematic of the experimental ANSIM setup.

**Transmission Electron Microscopy.** Solutions of #21−31 peptide were deposited onto carbon-coated 300-mesh transmission electron microscopy (TEM) grids (Ted Pella Inc., Redding, CA). After 2−3 min, the excess liquid was blotted away, and 1% phosphotungstic acid solution (pH 2.0) was deposited as a negative stain and blotted away. The transmission electron (TE) microscopy measurements were acquired using a Hitachi S-5200 (Japan) scanning electron microscope, with an acceleration voltage of 15 kV.

**Transmission FTIR Spectroscopy.** FTIR spectra (PerkinElmer, Waltham, MA) were obtained by depositing the fibril solutions onto $CaF_2$ substrates. The spectrum of a TMAO-TFA/water solution was also taken for comparison.

**Apertureless Near-Field Scanning Infrared Microscopy (ANSIM).** ANSIM measurements were done using a homemade device. The schematic of the experimental setup is shown in Figure 1. A multimode atomic force microscope (AFM) (Veeco Instruments, Santa Barbara, CA) was used for measuring the topography of the sample as well as for producing the near-field enhanced scattering modulated at the tip oscillation frequency. Tapping-mode, NSC14/Ti−Pt platinum-coated cantilevers (MicroMasch, Estonia) were used to enhance the scattering of the continuous wave, tunable (frequency range, 2100 to 1600 $cm^{-1}$) PL3 CO gas IR laser (Edinburgh Instruments, Great Britain) near the surface. A helium neon laser (Melles Griot, Albuquerque, NM) was used as a guide for the alignment of the invisible IR beam. The IR laser beam was directed toward a focusing lens after passing a ZnSe partial reflector and focused onto the apex of the oscillating AFM tip. The polarization of the beam was parallel to the long axis of the probe to enhance the scattered field. The backscattered IR radiation was then added to a reference homodyne field (reflected from a piezoelectric mounted mirror). A paraboloidal mirror was used to focus the interfered beam on a mercury cadmium telluride (MCT) infrared detector (Graseby Infrared, Orlando, FL). A single channel piezo driver (Thorlabs, Newton, NJ) was used to correct the relative phase of the homodyne reference beam to maximize the detected signal. The optical microscope was attached rigidly on a platform mounted atop a XYZ translational stage. The AC part of the detected signal was separated using a lock-in amplifier (model SR844 RF, Stanford Research Systems, Sunnyvale, CA) to demodulate the signal at the tip oscillation frequency from the static background. The scattering intensity was monitored as the AFM tip scanned over the surface and the topography data was obtained simultaneously. The software used for data and image collection was Nanoscope V5.31r1 (Veeco Instruments, Santa Barbara, CA). The image processing and data analysis software used was Igor Pro 6.04 (WaveMetrics, Portland, OR).

## RESULTS AND DISCUSSION

**Scanning Electron Microscopy and Fourier Transform Infrared Studies.** Two 1 mM solutions of #21−31 peptide were prepared in 10 mM TMAO, and the fibrils were studied using transmission electron microscopy (TEM). Figure 2A shows fibrils resulting from 5 days of incubation, and Figure 2B shows fibrils resulting from incubation for 1 month. Figure 2A demonstrates that after 5 days of incubation, the fibrils are observed to have smooth morphology that is characteristic of mature fibrils. After 1 month of incubation, mature fibrils are observed in bundles (Figure 2B), with different morphologies such as twists. This is similar to what has been observed in insulin fibrils.[49] The density of the fibrils in the solution is also increased compared to the sample shown in Figure 2A. It is seen in both images that structures with rough morphology previously reported as immature fibrils[50] are not observed.

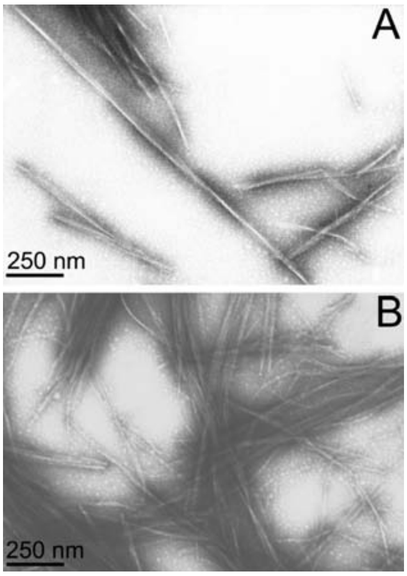

**Figure 2.** TEM images of the fibrils. (A) TEM image of fibrils from a 5 day old solution of 1 mM peptide in TMAO solution. (B) TEM image of fibrils from a 1 month old solution of 1 mM peptide in TMAO. Fibrils from the same solution were used in the near-field imaging experiments.

A representation of different structural stages of fibril formation at higher resolutions is given in Figure 3. Figure 3A shows an image of 1 month old solution of fibrils deposited onto an ultraflat gold substrate, obtained using tapping-mode AFM phase imaging. It is observed that different morphologies are present in the fibril structure; for example, some bundles are observed to be primarily made of straight fibrils. In Figure 3B, protofilaments similar to those reported by Jimenez et al.[49] for insulin fibrils are observed. In Figure 3Bi, the fibril shows a twisted, left-handed helical structure. In Figure 3Bii, the twisted fibril shows long ridges running parallel to the length of the fibril. This is likely due to the presence of thinner, smaller protofilaments that bundle together to form the smooth, mature fibril.[49] Thus, different morphologies are observed to exist at different stages of fibril formation. In Figure 3C, an illustration of the secondary structure of the #21−31 peptide protofilament is shown. Each horizontal line within the ladder-like structure represents one peptide chain, and the dotted line represents peptide pairing to the adjacent chain to form a $\beta$-sheet conformation. A detailed arrangement of the peptide chains is shown in Figure D. In Figure D, the chemical structure of the #21−31 peptide is shown along with two possible $\beta$-sheet secondary structure conformations using a pair of the polypeptide chains. The illustration on the top represents a parallel $\beta$-sheet secondary structure. Parallel $\beta$-sheet secondary structure is characterized by neighboring polypeptide

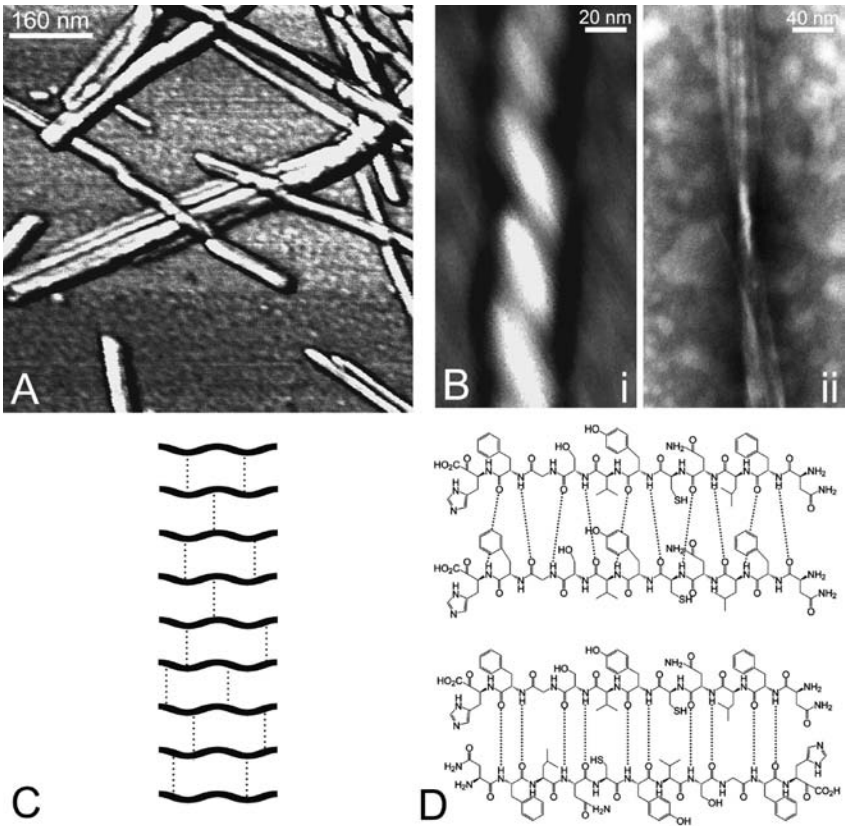

**Figure 3.** General summary of the fibril structure at increasing spatial resolution. (A) AFM phase image of a 1 month old fibril solution, composed of a bundle of several smaller, straight components. (B) (i) AFM phase image of a fibril twisting in a helical fashion. (ii) TEM image of a twisted fibril composed of several smaller protofilaments, as observed by the presence of straight ridges running parallel to the long axis of the fiber. (C) Illustration of the secondary structure adopted by the #21−31 peptide of $\beta_2$-m, with each horizontal rung on the ladder-like structure representing one peptide chain. (D) Arrangements of the #21−31 peptide of $\beta_2$-m, showing a pair of the peptide chains in a parallel $\beta$-sheet (top) or anti-parallel $\beta$-sheet (bottom) conformation.

chains traveling in the same direction. They are hydrogen-bonded to each other through a hydrogen atom covalently bound to a nitrogen on one peptide chain and a carboxy oxygen atom located on the partner chain. The illustration on the bottom represents anti-parallel $\beta$-sheet secondary structure and involves hydrogen-bonded, neighboring peptide chains traveling in opposite directions.[51]

Figure 4 depicts the FTIR absorption spectra obtained for fibrils in solutions with and without TMAO after 1 week of incubation at room temperature, as well as for mature fibrils formed in TMAO solution after 1 month of incubation. The spectra for the fibril solutions containing TMAO, independent of the incubation time, have peaks at 1630, 1665, and 1692 cm$^{-1}$. In contrast, the spectrum for the fibril solution without TMAO has peaks at 1630 and 1668 cm$^{-1}$ only. The peak locations within the amide I region (1600−1700 cm$^{-1}$) convey the type of secondary structure adopted by the fibrils. The peaks present at 1665 and 1668 cm$^{-1}$ correspond to $\beta$-turns[11] or $\beta$-bulge[14] present within the fibril morphology. The peak at 1630 cm$^{-1}$ indicates the presence of parallel[52] and/or anti-parallel[53,54] $\beta$-sheet structure within the sample. The peak at 1692 cm$^{-1}$ has two possible identities; it corresponds to either anti-parallel $\beta$-sheet structure or a TMAO−TFA complex.[55] However, in this work it does not denote the presence of anti-parallel $\beta$-sheet structure. The unusually intense and narrow high frequency 1692 cm$^{-1}$ peak is primarily due to a crystalline form of the TMAO−TFA complex. The FTIR spectrum of a 10:1 TMAO:TFA blank solution is shown in the Supporting Information. As will be described in the next section, it is interesting to note that using ANSIM, very few amyloid fibrils show decreased scattering of the IR radiation at 1691 cm$^{-1}$. Apparently the structure of particular

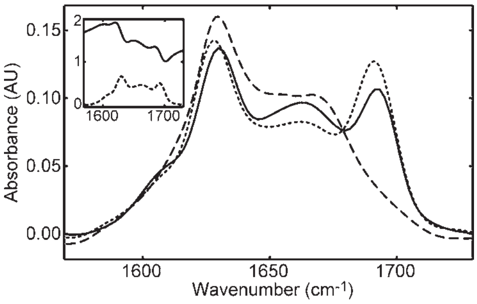

**Figure 4.** FTIR spectra of the #21−31 $\beta_2$-m amyloid fibrils. The solid black line represents fibrils from a 1 month old, 1 mM TFA peptide solution in the presence of TMAO, the dotted line is for fibrils from the 1 week old, 1 mM TFA peptide solution in TMAO, and the dashed line is for fibrils from a 1 week old, 1 mM TFA peptide solution. The inset shows the real and imaginary parts of the index of refraction of the spectrum of the 1 month old solution obtained using Kramers−Kronig transformation. The curves have been rescaled to have the same area underneath the main peak (1630 cm$^{-1}$).

amyloid fibrils predisposes the TMAO-TFA molecule to complex with the fibril. This last peak only appears in the TMAO-containing fibril solutions.

Anti-parallel $\beta$-sheet structure in a nearly identical peptide fragment has been reported previously; Lu et al.[34] have demonstrated that the IR spectrum collected for the #21−30 peptide shows a peak present at both 1628 and 1697 $\text{cm}^{-1}$, which could demonstrate the presence of anti-parallel $\beta$-sheet. The presence of anti-parallel $\beta$-sheet structure within other amyloid fibrils has been demonstrated previously by Petkova et al.[56] and Naito et al.[57] using solid-state NMR spectroscopy. We iterate, however, that anti-parallel $\beta$-sheet is not detectably responsible for the signal we observe at 1692 $\text{cm}^{-1}$. As shown in the Supporting Information section, the anti-parallel $\beta$-sheet contribution to the total $\beta$-sheet structure in bulk fibril measurements is limited to roughly 8%. The Supporting Information addresses this issue in some detail.

**Near-Field Spectroscopy Studies of Amyloid Fibrils.** To determine whether the heterogeneity of the fibril secondary structure bulk spectra varies among and/or within fibrils, IR imaging with high spatial resolution is needed. This is performed using ANSIM. Mueller et al. previously demonstrated the ability of ANSIM to detect the chemical composition and structural variation of a polymeric surface with a resolution of less than 30 nm.[15]

To calculate the expected scattered field spectrum, the index of refraction and the dielectric constants of the fibrils are required. The real and imaginary parts of the index of refraction were obtained using the Kramers−Kronig transformation of the absorption spectrum of the 1 month old fibrils (the inset of Figure 4). The imaginary part of the index of refraction is proportional to the absorption coefficient of the material.

$$K(\lambda) = \frac{\lambda \alpha(\lambda)}{4\pi L} \tag{1}$$

where $K$ is the imaginary part of the index as a function of wavelength ($\lambda$), $\alpha(\lambda)$ is the absorption spectrum, and $L$ is the path length of the beam. The real part of the index of refraction can then be obtained using the Kramers−Kronig relationship:[58]

$$N(\lambda) = n_b + \frac{2\lambda^2}{\pi} P \int \frac{K(\lambda')}{\lambda'(\lambda^2 - \lambda'^2)} \, d\lambda' \tag{2}$$

where $n_b$ is the index of refraction outside the FTIR spectrum (i.e., visible range), $N(\lambda)$ is the real part of the index of refraction as a function of wavelength, and $P$ denotes the Cauchy principal value, which defines the proper contour integrals. Once the complex index of refraction and thus the complex dielectric constant ($\varepsilon = n^2$) is calculated, the scattered field loss by the AFM-tip/protein-sample interface when the tip is positioned on top of the fibrils can be calculated using the coupled dipoles model.

The coupled dipoles model explains the origin of the chemical contrast present in the near-field IR imaging reasonably well.[19,26,59] As originally conceived by Knoll and Keilmann,[60] it strictly applies only to homogeneous samples extending further than the tip diameter, but Brehm et al.[26] found the phase shift of the scattered field above a virus particle yielded a spectrum similar to the far-field signature. Subsequent results on heterogeneous polymer films[15] have yielded a similar conclusion. A detailed calculation of the near-field measurement analysis is given in the Supporting Information. In this model, the AFM tip is assumed to be a sphere oscillating above the sample surface. The polarizability is calculated using the interaction between the dipole moment of the sphere and its image dipole located below the substrate surface. As the tip is moved further away from the surface the value of the polarizability falls to zero. The local field interaction of a sphere (with radius $a$, dielectric constant of tip $\varepsilon_t$, distance $d$ separation from a half-space, and dielectric constant of the sample $\varepsilon_s$) is described by the following effective polarizability:[59]

$$\alpha_\perp^{\text{eff}} = \frac{\alpha}{1 - \dfrac{\alpha\beta}{16\pi(a+d)^3}}; \quad \alpha = 4\pi a^3 \frac{\varepsilon_t - 1}{\varepsilon_t + 2} \text{ and}$$
$$\beta = \frac{\varepsilon_s - 1}{\varepsilon_s + 1} \tag{3}$$

In the equation above, $\alpha_\perp^{\text{eff}}$ is the effective polarizability of the sphere-surface geometry for the normal incident polarization of the infrared laser field. Although other authors[61] have included a $(1 + \beta)$ term in the numerator of the $\alpha_\perp^{\text{eff}}$ equation, we have excluded it, since $(1 + \beta)$ is approximately equal to 1 ($\beta \ll \alpha$) in our calculations.

The intensity at the detector, incorporating the homodyne reference field, is represented by

$$I \approx E_r E_s \cos(\theta_r - \theta_s) \cos(\Omega t) \tag{4}$$

where $E_r$ and $E_s$ represent the electric field of the reference and the scattered beams and $\theta_r$ and $\theta_s$ are the phase of the two beams, respectively. By applying Mie scattering theory, demodulating at the first harmonic of the AFM tip frequency ($\omega$), and adjusting the phase so that $\theta_r = \theta_s$ above the gold substrate, it can be shown that in the Rayleigh limit (where $a \ll \lambda$), the scattered field loss compared to the scattering from a bare gold substrate is proportional to the imaginary part of the effective polarizability of the deposited material:[59]

$$C_{\text{abs}} \propto k \,\text{Im}(\alpha_\perp^{\text{eff}}) \propto A \sin \varphi' \tag{5}$$

Using this equation the imaginary part of the effective polarizability is obtained for the fibril sample. $\varphi'$ represents the phase shift in the scattered field, where the phase of the reference field is set to be zero by the piezo at maximum scattering from the bare gold substrate.

To obtain the experimental scattered field, the scattering field is amplified by a reference field (homodyne amplification) collected by the infrared detector. There are two components to the signal, the low frequency DC component and the high frequency AC component. The latter signal is isolated using a lock-in amplifier, which is demodulated at the AFM tip oscillation frequency and represents the experimental scattered field. A detailed explanation of the near-field measurements is given in the Supporting Information.

To accurately measure the scattered field of the fibrils from the experimental near-field images, a histogram of the scattered field in the spatial region of interest was obtained. The histogram usually has a broad shoulder and is well-fitted with two distinct Gaussian curves. These two curves correspond to the scattered field distributions of the bare gold substrate and the fibril of interest. At each wavenumber, the peak-to-peak distance between the two Gaussians is taken as the difference between the scattered field of the bare gold substrate and the fibril. Thus, the experimental scattered field spectrum shown in Figure 5 was calculated using this procedure. This method provides a good representation of the experimental scattered field because the noise in the signal does not affect the measured scattering difference. As mentioned before, the phase of the homodyne field is set to maximize the scattering amplitude on areas with bare gold (gold scatters IR radiation with uniform efficiency across the frequencies probed). The loss of scattered field at an area with fibrils decreases the value of the scattered field propagated to the IR detector, which is due to changes of the phase value $\varphi'$.

Figure 5 (solid line, right axis) shows the near-field scattering spectrum calculated from the FTIR absorption spectrum. The ANSIM measurements were obtained in the 1600–1700 cm$^{-1}$ range. At each wavenumber where measurements were made, topography and near-field images were collected simultaneously. Figure 5 compares the calculated near-field spectrum (solid line) with the ANSIM measurements made in different spatial regions (dots connected by dashed lines), and a good correlations of peak positions is observed.

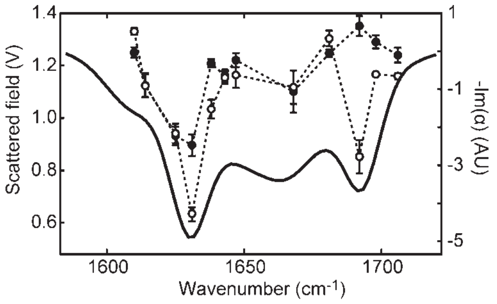

**Figure 5.** Calculated imaginary part of the effective polarizability (right *y*-axis, solid line) and experimental scattered field (left *y*-axis) as a function of wavenumber. The ANSIM scattered field spectra are obtained from fibril P1 with $\beta$-sheet secondary structure (●) and from fibril T1 with TMAO-TFA complex (○). The dashed lines are used to guide the eye.

Figure 6 shows ANSIM images collected at four different wavenumbers. Figure 6A represents a topography image collected simultaneously with a near-field image. The corresponding near-field images are illustrated in Figure 6B–E, where the numbers on the top left of the images indicates the specific IR wavenumber used. The near-field image shown in Figure 6B (1680 cm$^{-1}$) illustrates that fibrils of the same height scatter light to significantly different degrees, and therefore topography coupling is not the predominant origin of near-field contrast in the ANSIM measurements for the fibrils. A topography feature apparent in the center of the images is produced due to the heat induced by the AFM tip during the alignment of the infrared beam.

Each label on the image in Figure 6A represents one fibril. The labels indicate TMAO-TFA fibril complex (T) and parallel $\beta$-sheet conformation (P). Attenuation at 1691 cm$^{-1}$ could indicate anti-parallel $\beta$-sheet secondary structure[53] but is mainly due to TMAO-TFA fibril complex.[55] Attenuation at 1631 cm$^{-1}$ indicates the presence of parallel $\beta$-sheet secondary structure.[52] Attenuation at 1647 cm$^{-1}$ represents random coil secondary structure.[62] Attenuation at 1680 cm$^{-1}$ represents primarily undefined, disordered secondary structure.

Comparing Figure 6D (1631 cm$^{-1}$) and Figure 6E (1691 cm$^{-1}$), it is apparent that fibril T1 is mainly composed of TMAO-TFA fibril complex with parallel $\beta$-sheet secondary structure, whereas fibril P1 is composed of parallel $\beta$-sheet secondary structure. This is because P1 shows much lower scattering at 1631 cm$^{-1}$ but not at 1691 cm$^{-1}$, whereas T1 shows lower scattering at both wavenumbers. Similar assignments can be made for T2–T4 and P2–P5.

Experimental spectra have been collected for isolated fibrils (using the squared regions in Figure 6A) and compared with the calculated near-field spectrum in Figure 5. Though the topography of the two fibrils is very similar (the height of both fibrils is approximately 10 nm) and the fibrils are spatially only a

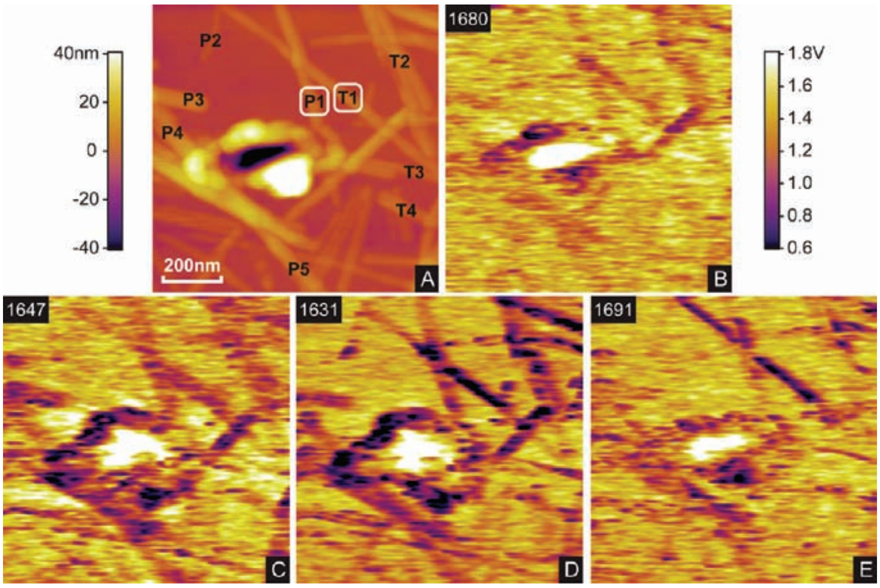

**Figure 6.** Experimental topography and near-field images collected at four different wavenumbers. Left scale: height in nanometers. Right scale: scattered field in lock-in voltage. (A) Topography image collected simultaneously with the near-field image obtained using 1691 cm$^{-1}$ radiation. The white boxes illustrate which parts of the fibrils were used to obtain the experimental scattered field spectra shown in Figure 5. The labels represent particular fibrils and are used to highlight the type of secondary structure conformation and composition each fibril has. (B, C, D, E) Corresponding near-field images collected at four different wavenumbers: 1680, 1647, 1631, and 1691 cm$^{-1}$.

few nanometers apart, their distinct and predicted spectra provide strong evidence of different compositions among different amyloid fibrils made from TMAO in solution.

Demirdoven et al. showed that the anti-parallel $\beta$-sheet has two IR active bands from the backbone carbonyls,[63] at approximately 1635 cm$^{-1}$ and approximately 1680 cm$^{-1}$. According to Hiramatsu and Kitagawa,[28] the transition dipole direction for the 1632 cm$^{-1}$ band for the amyloid fibril formed from the #21−31 peptide is approximately 27° relative to the long axis of the fibril. The 1680 cm$^{-1}$ band is expected to have a transition dipole direction approximately 65−70° to that of the 1632 cm$^{-1}$ band. The fibril is twisted (with variable pitch, depending on the fibril). Therefore, in our case, as a function of phase in the twist these transition dipoles at 1690 cm$^{-1}$ interact strongly with the *p*-polarized IR laser light. Given the gold substrate, *s*-polarized light excitation of surface transition dipoles is weakly or not at all observed. The angle between the direction of the IR light propagation and the fibril is not expected to have a consequence on the detection of anti-parallel $\beta$-sheet transition dipoles at 1690 cm$^{-1}$ if twisting is with a small enough pitch such that a fibril scatters uniformly along its axis. We note that our near-field IR findings are consistent with a fine pitch in the fibril twist, since the $\beta$-core twist is a common feature in amyloid fibrils[64] and the heights of the fibrils seen in Figure 6 are consistent with rapid twisting.

However, on balance, the fact that the anti-parallel $\beta$-sheet FTIR peak is expected to be much weaker than the parallel $\beta$-sheet FTIR peak (opposite to what is observed) leads us to conclude that, within the errors of our FTIR method, this observed spectral feature at 1691 cm$^{-1}$ is not due to anti-parallel $\beta$-sheet secondary structure, and additional evidence is provided by the presence of the 1690 cm$^{-1}$ peak in the FTIR spectrum of a 10:1 TMAO:TFA blank solution (in Supporting Information). However, as stated previously, it is likely that particular morphological structures adopted by particular mature amyloid fibrils may be inclined to bind or complex TMAO−TFA more strongly than others. We note that the concentration of TMAO we employed (10 mM) is close to the range observed during renal failure (~5 mM).[39,65] We speculate that the possible structure variations observed among individual amyloid fibrils may result in different mechanical properties of the fibrils.[66]

In summary, the #21−31 fragment of $\beta_2$-microglobulin amyloid fibril formation studies was utilized, and it has been shown that the addition of TMAO causes some fibrils to contain TMAO. This novel finding was further advanced with the implementation of near-field scanning IR microscopy, which is a specialized technique used to obtain secondary structure information of individual fibrils with a spatial resolution better than 30 nm, and it was found that composition heterogeneity is evident at the single fibril level. The ability to detect the composition variations and secondary structure with such high spatial resolution enables the study of the properties of individual fibrils, which in turn may lead to new approaches into studies of the dynamics of fibril formation.

## ASSOCIATED CONTENT

**Supporting Information.** Characterization of the amyloid fibrils via circular dichroism, UV−vis, and FTIR spectroscopy synthesized with and without TMAO, creatinine, and urea and details of the experimental near-field measurement. This material is available free of charge via the Internet at http://pubs.acs.org.

## AUTHOR INFORMATION

### Corresponding Author

Phone: 416-946-8401. Fax: 416-946-3649. E-mail: gwalker@chem.utoronto.ca.

## ACKNOWLEDGMENT

We thank Raymond Yurko, Peptide Synthesis Core Group, Center for Biotechnology and Bioengineering, University of Pittsburgh for the synthesis of the peptide fragment, Matt Kofke for help with the use of the electron-beam evaporator at the University of Pittsburgh, Ilya Gourevich for help in the SEM/STEM experiments, James K. Li for comments on an early draft of the manuscript, ANALEST lab (University of Toronto), Dr. Al-Amin Dhirani for the use of the FTIR spectrometer, and Dr. Ronald Kluger for the use of the CD spectrometer. We acknowledge NIH, NSF, NSERC, ARO, and CIHR for financial support.

## REFERENCES

(1) Luheshi, L. M.; Crowther, D. C.; Dobson, C. M. *Curr. Opin. Chem. Biol.* **2008**, *12*, 25–31.

(2) Lu, X.; Wintrode, P. L.; Surewicz, W. K. *Proc. Natl. Acad. Sci. U.S.A.* **2007**, *104*, 1510–1515.

(3) Hizume, M.; Kobayashi, A.; Teruya, K.; Ohashi, H.; Ironside, J. W.; Mohri, S.; Kitamoto, T. *J. Biol. Chem.* **2009**, *284*, 3603–3609.

(4) Kozhukh, G. V.; Hagihara, Y.; Kawakami, T.; Hasegawa, K.; Naiki, H.; Goto, Y. *J. Biol. Chem.* **2002**, *277*, 1310–1315.

(5) Gras, S. L.; Tickler, A. K.; Squires, A. M.; Devlin, G. L.; Horton, M. A.; Dobson, C. M.; MacPhee, C. E. *Biomaterials* **2008**, *29*, 1553–1562.

(6) Serpell, L. C.; Sunde, M.; Benson, M. D.; Tennent, G. A.; Pepys, M. B.; Fraser, P. E. *J. Mol. Biol.* **2000**, *300*, 1033–1039.

(7) Paravastu, A. K.; Qahwash, I.; Leapman, R. D.; Meredith, S. C.; Tycko, R. *Proc. Natl. Acad. Sci. U.S.A.* **2009**, *106*, 7443–7448.

(8) Stopa, B.; Piekarska, B.; Konieczny, L.; Rybarska, J.; Spolnik, P.; Zemanek, G.; Roterman, I.; Krol, M. *Acta Biochim. Pol.* **2003**, *50*, 1213–1227.

(9) Ivanova, M. I.; Sawaya, M. R.; Gingery, M.; Attinger, A.; Eisenberg, D. *Proc. Natl. Acad. Sci. U.S.A.* **2004**, *101*, 10584–10589.

(10) Hasegawa, K.; Ohhashi, Y.; Yamaguchi, I.; Takahashi, N.; Tsutsumi, S.; Goto, Y.; Gejyo, F.; Naiki, H. *Biochem. Biophys. Res. Commun.* **2003**, *304*, 101–106.

(11) Hiramatsu, H. H.; Goto, Y.; Naiki, H.; Kitagawa, T. *J. Am. Chem. Soc.* **2004**, *126*, 3008–3009.

(12) Byler, D. M.; Susi, H. *Biopolymers* **1986**, *25*, 469–487.

(13) Fabian, H.; Gast, K.; Laue, M.; Misselwitz, R.; Uchanska-Ziegler, B.; Ziegler, A.; Naumann, D. *Biochemistry* **2008**, *47*, 6895–6906.

(14) Hiramatsu, H.; Goto, Y.; Naiki, H.; Kitagawa, T. *J. Am. Chem. Soc.* **2005**, *127*, 7988–7989.

(15) Mueller, K.; Yang, X.; Paulite, M.; Fakhraai, Z.; Gunari, N.; Walker, G. C. *Langmuir* **2008**, *24*, 6946–6951.

(16) Lahrech, A.; Bachelot, R.; Gleyzes, P.; Boccara, A. C. *Opt. Lett.* **1996**, *21*, 1315–1317.

(17) Taubner, T.; Hillenbrand, R.; Keilmann, F. *J. Microsc.* **2003**, *210*, 311–314.

(18) Kim, Z. H.; Leone, S. R. *Opt. Express* **2008**, *16*, 1733–1741.

(19) Bridger, P. M.; McGill, T. C. *Opt. Lett.* **1999**, *24*, 1005–1007.

(20) Stebounova, L.; Akhremitchev, B. B.; Walker, G. C. *Rev. Sci. Instrum.* **2003**, *74*, 3670–3674.

(21) Akhremitchev, B. B.; Pollack, S.; Walker, G. C. *Langmuir* **2001**, *17*, 2774–2781.

(22) Hecht, B.; Bielefeldt, H.; Inouye, Y.; Pohl, D. W.; Novotny, L. *J. Appl. Phys.* **1997**, *81*, 2492–2498.

(23) Labardi, M.; Patane, S.; Allegrini, M. *Appl. Phys. Lett.* **2000**, *77*, 621–623.

(24) Palanker, D. V.; Simanovskii, D. M.; Huie, P.; Smith, T. I. *J. Appl. Phys.* **2000**, *88*, 6808–6814.

(25) Akhremitchev, B. B.; Sun, Y.; Stebounova, L.; Walker, G. C. *Langmuir* **2002**, *18*, 5325–5328.

(26) Brehm, M.; Taubner, T.; Hillenbrand, R.; Keilmann, F. *Nano Lett.* **2006**, *6*, 1307–1310.

(27) Dazzi, A.; Prazeres, R.; Glotin, F.; Ortega, J. M. *Ultramicroscopy* **2007**, *107*, 1194–1200.

(28) Hiramatsu, H.; Kitagawa, T. *Biochim. Biophys. Acta* **2005**, *1753*, 100–107.

(29) Gazit, E. *Angew. Chem., Int. Ed.* **2002**, *41*, 257–259.

(30) Xu, S. *Amyloid* **2007**, *14*, 119–131.

(31) Naiki, H.; Hashimoto, N.; Suzuki, S.; Kimura, H.; Nakakuki, K.; Gejyo, F. *Amyloid: Int. J. Exp. Clin. Invest.* **1997**, *4*, 223–232.

(32) Naiki, H.; Hasegawa, K.; Yamaguchi, I.; Nakamura, H.; Gejyo, F.; Nakakuki, K. *Biochemistry* **1998**, *37*, 17882–17889.

(33) Naiki, H.; Gejyo, F. *Methods Enzymol.* **1999**, *309*, 305–318.

(34) Lu, M.; Hiramatsu, H.; Goto, Y.; Kitagawa, T. *J. Mol. Biol.* **2006**, *362*, 355–364.

(35) Linse, S.; Cabaleiro-Lago, C.; Xue, W. F.; Lynch, I.; Lindman, S.; Thulin, E.; Radford, S. E.; Dawson, K. A. *Proc. Natl. Acad. Sci. U.S.A.* **2007**, *104*, 8691–8696.

(36) Yang, D. S.; Yip, C. M.; Huang, T. H. J.; Chakrabartty, A.; Fraser, P. E. *J. Biol. Chem.* **1999**, *274*, 32970–32974.

(37) Bolen, D. W.; Baskakov, I. V. *J. Mol. Biol.* **2001**, *310*, 955–963.

(38) Kim, Y.-S.; Jones, L. S.; Dong, A.; Kendrick, B. S.; Chang, B. S.; Manning, M. C.; Randolph, T. W.; Carpenter, J. F. *Protein Sci.* **2003**, *12*, 1252–1261.

(39) Foxall, P. J. D.; Mellotte, G. J.; Bending, M. R.; Lindon, J. C.; Nicholson, J. K. *Kidney Int.* **1993**, *43*, 234–245.

(40) Schrieber, R. *Semin. Dial.* **2002**, *15*, 71–72.

(41) Wishart, D. S. *Am. J. Transplant.* **2005**, *5*, 2814–2820.

(42) Fink, A. L. *Acc. Chem. Res.* **2006**, *39*, 628–634.

(43) Tatzelt, J.; Prusiner, S. B.; Welch, W. J. *EMBO J.* **1996**, *15*, 6363–6373.

(44) Knowles, T. P. J.; Shu, W.; Devlin, G. L.; Meehan, S.; Auer, S.; Dobson, C. M.; Welland, M. E. *Proc. Natl. Acad. Sci. U.S.A.* **2007**, *104*, 10016–10021.

(45) Wang, A.; Bolen, D. W. *Biochemistry* **1997**, *36*, 9101–9108.

(46) Lin, T. Y.; Timasheff, S. N. *Biochemistry* **1994**, *33*, 12695–12701.

(47) Smith, M. J.; Crowther, R. A.; Goedert, M. *FEBS Lett.* **2000**, *484*, 265–270.

(48) Meadows, P. Y.; Walker, G. C. *Langmuir* **2005**, *21*, 4096–4107.

(49) Jimenez, J. L.; Nettleton, E. J.; Bouchard, M.; Robinson, C. V.; Dobson, C. M. *Proc. Natl. Acad. Sci. U.S.A.* **2002**, *99*, 9196–9201.

(50) Kad, N. M.; Thomson, N. H.; Smith, D. P.; Smith, D. A.; Radford, S. E. *J. Mol. Biol.* **2001**, *313*, 559–571.

(51) Voet, D.; Voet, J. G. *Biochemistry*; Wiley: New Jersey, 2004.

(52) Chirgadze, Y. N.; Nevskaya, N. A. *Biopolymers* **1976**, *15*, 627–636.

(53) Chirgadze, Y. N.; Nevskaya, N. A. *Biopolymers* **1976**, *15*, 607–625.

(54) Kubelka, J.; Keiderling, T. A. *J. Am. Chem. Soc.* **2001**, *123*, 12048–12058.

(55) Boehner, U.; Zundel, G. *J. Phys. Chem.* **1986**, *90*, 964–973.

(56) Petkova, A. T.; Buntkowsky, F.; Dyda, R. D.; Leapman, W. M.; Tycko, R. *J. Mol. Biol.* **2004**, *335*, 247–260.

(57) Naito, A.; Kamihira, M.; Inoue, R.; Saito, H. *Magn. Reson. Chem.* **2004**, *42*, 247–257.

(58) Arfken, G. *Mathematical Methods for Physicists*; Academic: Boston, 1958.

(59) Knoll, B.; Keilmann, F. *Opt. Commun.* **2000**, *182*, 321–328.

(60) Knoll, B.; Keilmann, F. *Nature* **1999**, *399*, 134–137.

(61) Raschke, M. B.; Lienau, C. *Appl. Phys. Lett.* **2003**, *83*, 5089–5091.

(62) Zurdo, J.; Guijarro, J. I.; Dobson, C. M. *J. Am. Chem. Soc.* **2001**, *123*, 8141–8142.

(63) Demirdoven, N.; Cheatum, C. M.; Chung, H. S.; Khalil, M.; Knoester, J.; Tokmakoff, A. *J. Am. Chem. Soc.* **2004**, *126*, 7981–7990.

(64) Sunde, M.; Serpell, L. C.; Bartlam, M.; Fraser, P. E.; Pepys, M. B.; Blake, C. C. F. *J. Mol. Biol.* **1997**, *273*, 729–739.

(65) Serkova, N.; Fuller, T. F.; Klawitter, J.; Freise, C. E.; Niemann, C. U. *Kidney Int.* **2005**, *67*, 1142–1151.

(66) Guo, S.; Akhremitchev, B. B. *Biomacromolecules* **2006**, *7*, 1630–1636.